Dispersion processes in weakly dissipative estuaries: Part 2. Multiple constituent tides.

A. De Leo[1], N. Tambroni[1], and A. Stocchino[2]

[1]Dipartimento di Ingegneria Civile, Chimica e Ambientale, Università degli Studi di Genova, via Montallegro 1, 16145, Genova, Italia
[2]Department of Civil and Environmental Engineering, Hong Kong Polytechnic University, Hung Hom, Kowloon, Hong Kong

Key Points:

- The harmonic content of the tidal waves controls the generation of macro-vortices at the tidal inlet inducing vortices at different scales
- For the present tidal setting, longitudinal dispersion is enhanced in mixed tides with semi-diurnal constituent dominance
- Dispersion processes are dominated by non-local dynamics for particle separations larger than the typical injection scale.

Corresponding author: Annalisa De Leo, annalisa.deleo@edu.unige.it

Abstract

In the present study, we extend the analysis of the dispersion processes induced by tidal flow in weakly-dissipative estuaries discussed in the companion paper. Here we focus the attention on the flow induced by more realistic tidal waves provided by different combinations of semi-diurnal and diurnal constituents. We employ a large-scale physical model of a system composed by a large basin (open sea) and a compound tidal channel, where tides are produced as volume waves with prescribed shapes. Two-dimensional superficial velocity fields are used to study the main Eulerian and Lagrangian properties of the flow, in terms of absolute and relative particle statistics. The results suggest that the mixed character of the tides strongly influences the shape of the macro-vortices generated at the tidal inlet, whereas the overall residual currents seem to be less sensitive. Moreover, for the present tidal setting, longitudinal dispersion, the dominant dispersion process, is enhanced when the semi-diurnal constituents prevail. Finally, multiple particle statistics show regimes typical of non-local dynamics for particle separation larger than a typical injection length scale, which is the size of the tidal inlet. Non-local dynamics imply that the dispersion is dominated by flow structures larger than the mean separation length, i.e. the tidal wavelength and the size of the macro-vortices. The present results together with those discussed in Part 1, offer a thorough insight in the main dispersion processes induced by tidal flows, which are extremely relevant in the case of estuarine dynamics.

Plain Language Summary

Tides are generated by combined astronomical forces among Earth, Moon and Sun. Unbalance between gravitational attraction and centrifugal force is the driving mechanism for ocean tides. Interestingly tides are composed by several constituents that can be mainly grouped in semi-diurnal (lunar and solar) and diurnal (lunar and solar) constituents. The presence of several harmonics dramatically influences the shape of the astronomical tide, whose form also changes during its propagation in shallow confined regions like coastal areas and estuaries. Here we are interested to understand how the shape of the tidal wave can influence the dispersion processes that occur in real estuaries. To this end we employ a large-scale laboratory model of an estuary and consider the flow generated by different tidal forcings, composed by semi-diurnal and diurnal constituents with varying phase lag and relative amplitude. Free surface velocity measurements are used to evaluate the main features of the transport processes, mainly related to longitudinal dispersion. Our results suggest that the mixed character of the tides may play an important role on the dispersion processes, enhancing the ability of the flow to transport mass in the main flow direction.

1 Introduction

Estuaries are considered transitional regions between landward waters and open sea, and thus important sites for human development. Estuarine regions can be classified depending on morphology, geometry configurations, vertical salinity stratification and finally hydrodynamics (Valle-Levinson, 2010). In particular, coastal bays and estuaries are characterized by flows mainly owed to hydraulic unbalance such as baroclinic pressure gradients, river inflows and wind stresses. If on one hand, tidal propagation has been deeply studied in order to better understand the suitable parameter to describe it (Seminara et al., 2010; Toffolon et al., 2006; Cai et al., 2012), on the contrary, less is known about the role of tidal circulation on transport processes. Tides are long-period waves induced by gravitational force unbalanced among Earth, Moon and Sun. In particular, astronomical tides are composed by several tide constituents, with different amplitude and periods, yielding to complex tidal waves (Lee & Chang, 2019). Moreover, daily and seasonal variations might occur depending on the combination of the main constituents.

Several studies focus on the definition of the time scales and the estimation of the dispersion coefficients in monochromatic tidal force conditions (see Cucco et al., 2009; Umgiesser et al., 2014; Viero & Defina, 2016, among others). At the same time, several studies have been dedicated to the prediction of multi-harmonic tides (Amin, 1986; Lee & Chang, 2019) and their propagation (Jay, 1991; Seminara et al., 2010; Fortunato & Oliveira, 2005; Toffolon et al., 2006; Cai et al., 2012). However, the investigation of the effects of multiple harmonics on the flow field and dispersion processes lacks of evidence. In fact, field studies devoted to the estimate of longitudinal dispersion coefficients (Monismith et al., 2002; Lewis & Uncles, 2003; Banas et al., 2004) did not provide a relationship among the coefficients and the tide wave shape. In the companion paper, Part 1, we focused our attention on the description of the flow field generated by a single harmonic tide on a large scale physical model of a basin, representing the open ocean, connected to a compound tidal channel through an inlet entrance. The aim was to asses a detailed Lagrangian description of the typical integral scales and single particle statistics, varying the controlling parameters in a simplified tidal forcing range. Dispersion coefficients have been evaluated and discussed as a function of the main external parameters following Toffolon et al. (2006). Employing the same experimental set up and the same Large Scale Particle Image Velocimetry technique, this second part of the work is devoted to extend the Lagrangian analysis to a more realistic context, i.e. tides composed by the contemporary coexistence of semi-diurnal and diurnal constituents. The flow structures are expected to be more complicated by the presence of multiple harmonics with possible effects on the main dispersion processes (Zimmerman, 1986). To assess the interplay of flow structures at different scales and the resulting dispersion regimes, multiple particle statistics have proven to be an effective analysis when applied to geophysical flows (LaCasce, 2008). In fact, the theoretical results in terms of relative dispersion and Finite Size Lyapunov Exponents suggest the possible existence of local and non-local dynamical behaviors (Kraichnan, 1966; Lin, 1972; Bennett, 1984; Babiano et al., 1990). The latter regimes are associated to particle separations that are influenced by different flow scales. Applications to geophysical flows showed the existence of both regimes when the flow is mainly generated by the tides (Enrile et al., 2019). In the present study, we will perform multiple particles statistics based on the measured flow fields of both the single harmonic case as well in the case of multiple harmonics tides.

The paper starts with a brief description of the experimental apparatus, already discussed in detail in Part 1; a characterization of the tidal forcing employed follows. In Section 3, we asses the governing parameters and describe the tidal propagation that occurs within the physical model. Eulerian and Lagrangian analysis follows describing in details the flow characteristics, identifying vortical structures using the Okubo-Weiss parameter (Okubo, 1970) and evaluating the influence of the initial conditions on the Lagrangian scales. A comparison of the multiple particle statistics and Finite-Size Lyapunov Exponent (FSLE) between Part 1 and Part 2 is then provided.

2 Experimental Methods

2.1 Laboratory set-up and measuring technique

We employ the same experimental apparatus and measuring techniques adopted for the single-component tide experiments described in the companion paper, Part 1. Here we briefly recall the main features of the laboratory apparatus. Our main goal is to measure two dimensional velocity fields on the free surface layer induced by a controlled tidal oscillation in a large scale shallow flume. The flume is approximately 29 m long and 2.42 m wide. At one end a cylinder is free to oscillate in a feeding tank according to a prescribed time law in order to produce a tidal wave. The latter then propagates in a 6 m long rectangular channel before crossing a tidal inlet at the beginning of a 23 m compound channel. The channel cross section is composed by a 0.24 m deep main channel and two lateral tidal flats. Moreover, the main channel has a longitudinal slope of about

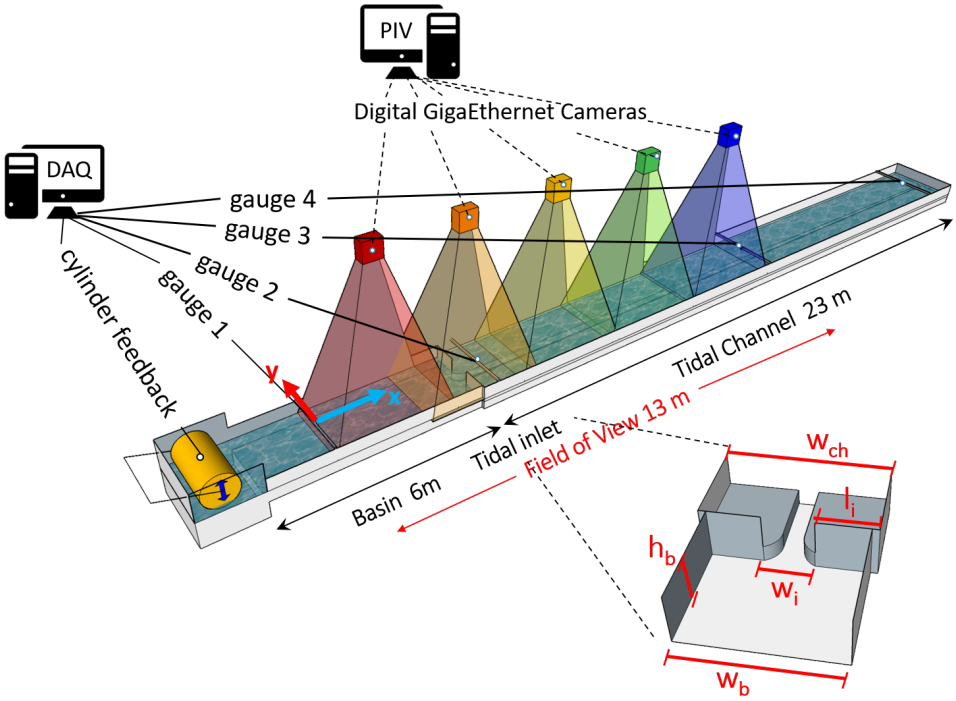

Figure 1. Sketch of the experimental set up and measuring systems.

2.5‰ and an exponentially landward decreasing width (w_i), varying from about 70 cm at the tidal inlet to about 11 cm at its closed end. Consequently, the tidal flats width ranges between 0.86 m and 1.16 m on each side. Figure 1 shows a sketch of the experimental flume and setup. Two dimensional superficial velocity fields $\mathbf{u}(\mathbf{x},t) = (u(\mathbf{x},t), v(\mathbf{x},t))$ have been measured using a Particle Image Velocimetry equipment specifically designed for the present purpose to obtain a large field of measurements, approximately 13 m $\times$ 3 m. The image acquisition system is composed by five digital cameras (Teledyne Dalsa Genie Nano 4 of model C1280 and 1 of model C2450). The system allowed us to record at a frequency of 10 Hz. The images, obtained after a pre-processing providing a single image for each instant, have been analysed using the software proVision-XS^{TM} (Integrated Design Tools Inc). Finally, free surface elevation has been monitored at four control points along the entire channel using ultrasound gauges (Honeywell model 946-A4V-2D-2C0-380E, with 30 cm range and an accuracy of 0.2% of the full scale). More details are provided in the companion paper.

2.2 Multiple constituents tidal forcing generation

Differently from the experiments described in the Part 1, here we have considered a more complex tidal forcing composed of different harmonics. Astronomical tide is indeed provided by a wide variety of harmonic constituents each one associated to a different gravitational force interaction between Earth, Moon and Sun. In terms of amplitude, the first four main tidal contributions are: the principal lunar semi-diurnal (M_2, 12.42 hr period), the principal lunar diurnal (K_1, 23.93 hr), the principal solar semi-diurnal (S_2, 12 hr period), and the principal solar diurnal (O_1, 25.82 hr). Grouping together the diurnal and semidiurnal components a simplified form for the astronomical tidal free sur-

Table 1. Experimental forcing tide parameters

	exp	T_{sd}[s]	T_d [s]	a_{sd}[m]	a_d[m]	ϕ [m]	F
	001	100	200	0.0042	0.00016	0	0.04
series 1	002	100	200	0.003	0.0006	0	0.20
	003	100	200	0.003	0.0009	0	0.30
	004	100	200	0.003	0.0013	0	0.44
	005	100	200	0.0022	0.00185	0	0.84
	006	100	200	0.0018	0.0022	0	1.20
	007	100	200	0.0014	0.0025	0	1.69
series 2	008	100	200	0.003	0.0006	$-\pi/4$	0.20
	009	100	200	0.003	0.0009	$-\pi/4$	0.30
	010	100	200	0.003	0.0013	$-\pi/4$	0.44
	011	100	200	0.0022	0.00185	$-\pi/4$	0.84
	012	100	200	0.0018	0.0022	$-\pi/4$	1.20
	013	100	200	0.0014	0.0025	$-\pi/4$	1.69
series 3	014	100	200	0.003	0.0006	$\pi/4$	0.20
	015	100	200	0.003	0.0009	$\pi/4$	0.30
	016	100	200	0.003	0.0013	$\pi/4$	0.44
	017	100	200	0.0022	0.00185	$\pi/4$	0.84
	018	100	200	0.0018	0.0022	$\pi/4$	1.20
	019	100	200	0.0014	0.0025	$\pi/4$	1.69

face oscillation reads:

$$\eta(t) = (A_{M2} + A_{S2}) \sin(\omega t) + (A_{K1} + A_{O1}) \sin(\frac{\omega}{2} t + \phi) = a_{sd} \sin(\omega t) + a_d \sin(\frac{\omega}{2} t + \phi) \quad (1)$$

where η is the free surface elevation, ω is the tidal angular frequency related to the semidiurnal tidal period T=12 hr and ϕ is the phase shift. The reasons that induce us to use a simplified form will be explained later on. The relative importance of the semi-diurnal and diurnal components can be expressed through the form factor F defined as (Lee & Chang, 2019):

$$F = \frac{A_{K1} + A_{O1}}{A_{M2} + A_{S2}} = \frac{a_d}{a_{sd}} \quad (2)$$

The form parameter can be used to discriminate the different types of astronomical tide, in particular:

- if $F < 0.25$, the tide is semi-diurnal;
- if $0.25 < F < 1.25$, the tide is mixed, but mainly semi-diurnal;
- if $1.25 < F < 3.0$, the tide is mixed, but mainly diurnal;
- if $F > 3.0$, the tide is diurnal.

According to Tsimplis et al. (1995) the form parameter associated with the astronomical tide observed in different places in the Mediterranean Sea spans over a wide range of values. As shown in Table 1, in our experiments we have thus considered different tidal forcings with form parameter varying between 0.038 and 1.7. Note that in our laboratory model we have investigated the role of diurnal and semidiurnal tides by imposing free surface oscillations according to (1). Hence, only two tidal periods have been set, one for the semi-diurnal constituents (T_{sd}) and one for the diurnal constituents ($2T_{sd}$), which are exactly multiple of each other. We acknowledge that observed semi-diurnal (M_2, S_2) and diurnal (K_1, O_1) are characterized by different periods and this difference

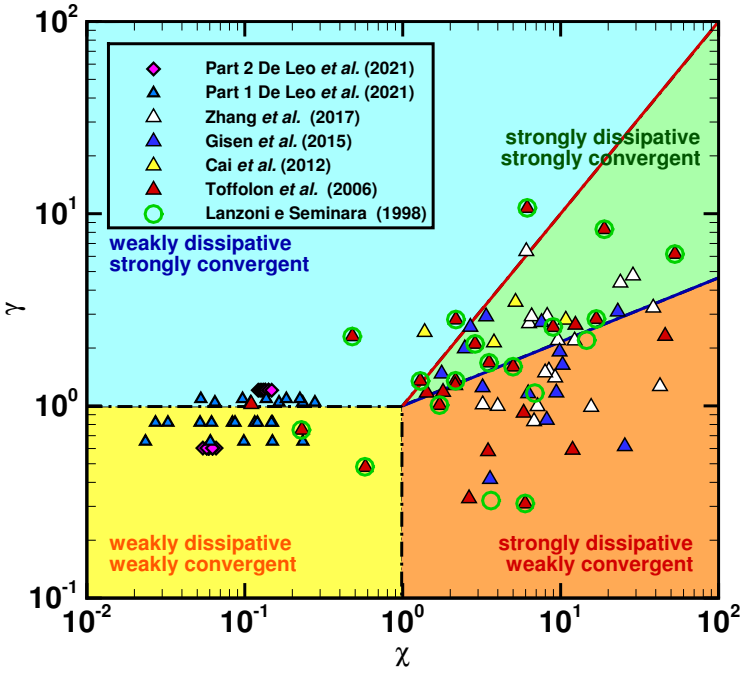

Figure 2. (χ, γ)-plane classification of the present experiments, experiments of Part 1 and of field observations as reported in Lanzoni and Seminara (1998), Toffolon et al. (2006), Cai et al. (2012) Gisen and Savenije (2015) and (Zhang & Savenije, 2017). $\gamma = \chi$ boundary (thick red line) and the $\gamma = \chi^{1/3}$ law (thick blue solid line) are also reported.

in periods leads to mixed tidal patterns with weekly variations (spring tide - neap tide cycles). However, reproducing this process at laboratory scales would have implied the acquisition of an unmanageable number of images, since our statistics are based on the average of several periods of the slowest modulation. Moreover, the phase shift introduced in equation (1) has been varied to understand the role of the tidal wave shape depending of the phase lag between the semi-diurnal and diurnal constituents. Three series of experiments have been performed for a total of 19 experiments varying the form factor F and the phase ϕ, see Table 1 for the relevant experimental parameters. In particular, a first series of experiments (experiments from 2 to 7) has been designed for different values of the form factor and vanishing phase. A second series (from experiment 8 to 13) has been performed for the same form factor of the first series, but choosing $\phi = -\pi/4$. The phase shifts has been changed to $\phi = \pi/4$ in the final series (from experiment 14 to 19) of experiments. Note that the limiting cases of strongly semi-diurnal tides (experiment 1, for instance) or strongly diurnal tides ($F > 1.7$) have been extensively discussed in the companion paper, referring to the single harmonic case.

3 Governing parameters and tidal propagation

In this section, we describe the external parameters that have been used to differentiate the experiments. The first non dimensional parameter that will be used is the form factor F, see equation 2, as introduced by Lee and Chang (2019), describing the semi-diurnal or diurnal dominance. However, the introduction of multiple constituents as analytically represented by equation (1) is chacterized by the presence of two differ-

ent tidal periods, thus raising problems when one typical time scale must be selected. Indeed, the use of the external parameters introduced in Part 1 for the monochromatic tide experiments is here complicate. Let us recall that in the compainon paper, following Toffolon et al. (2006), we have considered as external parameters the convergence ratio γ, and the friction parameter χ, defined as the ratio between frictional forces and inertial forces. They read:

$$\gamma = \frac{L_g}{2\pi L_b}, \qquad \chi = \epsilon \frac{L_g}{2\pi C^2 R_h}, \qquad \text{with} \qquad L_g = T\sqrt{gR_h}, \tag{3}$$

where $\epsilon = a/R_h$ is the non dimensional tidal amplitude, R_h is the hydraulic radius, L_b the convergence length and T the tidal period. Thus, they require the identification of a typical relative tidal amplitude ϵ and a tidal period T. The choice for the latter scales is straightforward when a monochromatic tide is considered, whereas in the simultaneous presence of more than one constituent it requires care. Note that Toffolon et al. (2006) and later Cai et al. (2012) applied their models to realistic estuaries where tides are formed by lunar and solar constituents with different periods, but dominated by the semi-diurnal lunar tide M_2. In the present study, we set the non dimensional tidal amplitude as the ratio between half the tidal excursion, defined as the difference between the highest and lowest water level and the hydraulic radius. We recall that all the three series of experiments have been designed in order to maintain the same tidal range, whilst varying the form factor and the phase shift. As far as the typical tidal period is concerned, we select the dominant period as the one of the higher amplitude constituent. Thus, the friction parameter χ has been calculated the latter. The values of the three series of experiments have been reported in the $(\gamma;\chi)-$plane plot shown in Figure 2 together with the experiments discussed in Part 1 and several field observations (Lanzoni & Seminara, 1998; Toffolon et al., 2006; Cai et al., 2012; Gisen & Savenije, 2015; Zhang & Savenije, 2017). As expected, the values of the χ parameter of all the present experiments are grouped around two values, since the amplitude is the same except for an obvious small experimental variation and the dominant tidal periods are two. Similarly to experiments of Part 1, our experimental model is representative of a weakly convergent-weakly dissipative estuary as described by Toffolon et al. (2006). It is now interesting to observe how the imposed tidal signals with different shapes (different form factor F) propagate from the flume basin (open sea condition) through the tidal inlet and along the compound channel. It is well known that nonlinearity is able to amplify the tidal wave amplitude and to produce higher harmonics, even with simple tidal wave forms (Lanzoni & Seminara, 1998; Toffolon et al., 2006). The theoretical model by Toffolon et al. (2006) showed how the marginal conditions for tidal wave amplification in estuaries may be strongly affected by the amplitude of tidal wave depending on the external parameters γ and χ. The marginal conditions have been provided as $\gamma = k\chi^m$, where the coefficients k and m strongly depend on the relative tidal amplitude. For the parameters γ and χ, and the relative amplitude ϵ of the present experiments, the theoretical model by Toffolon et al. (2006) predicts amplification of the tidal waves. Three examples of tidal propagation are shown in Figure 3. In particular, they refer to experiment 2 ($F = 0.2$ semi-diurnal tide), experiment 4 ($F = 0.444$, mixed tide mainly semi-diurnal) and experiment 7 ($F = 1.686$, mixed tide mainly diurnal). Panels a), b) and c) report water level measurements in the middle of three channel cross sections (see Figure 1 for the gauge positions) along the flume; the corresponding FFT analysis is plotted in panels d), e) and f). As expected tidal amplification is observed in all the cases leading to amplitudes in the tidal channel far from the inlet, even three times higher than at the flume basin (forcing wave). Note that in general, in agreement with the linear theory predictions for weakly convergent and weakly dissipative estuaries, both the diurnal and semidiurnal components amplify. However, the semidiurnal component is subject to a larger amplification than the diurnal one, this is related both to non-linearities and also to the occurrence that the mode associated to the semidiurnal component is closer to the resonant mode of our experimental model than the one associated to the diurnal component.

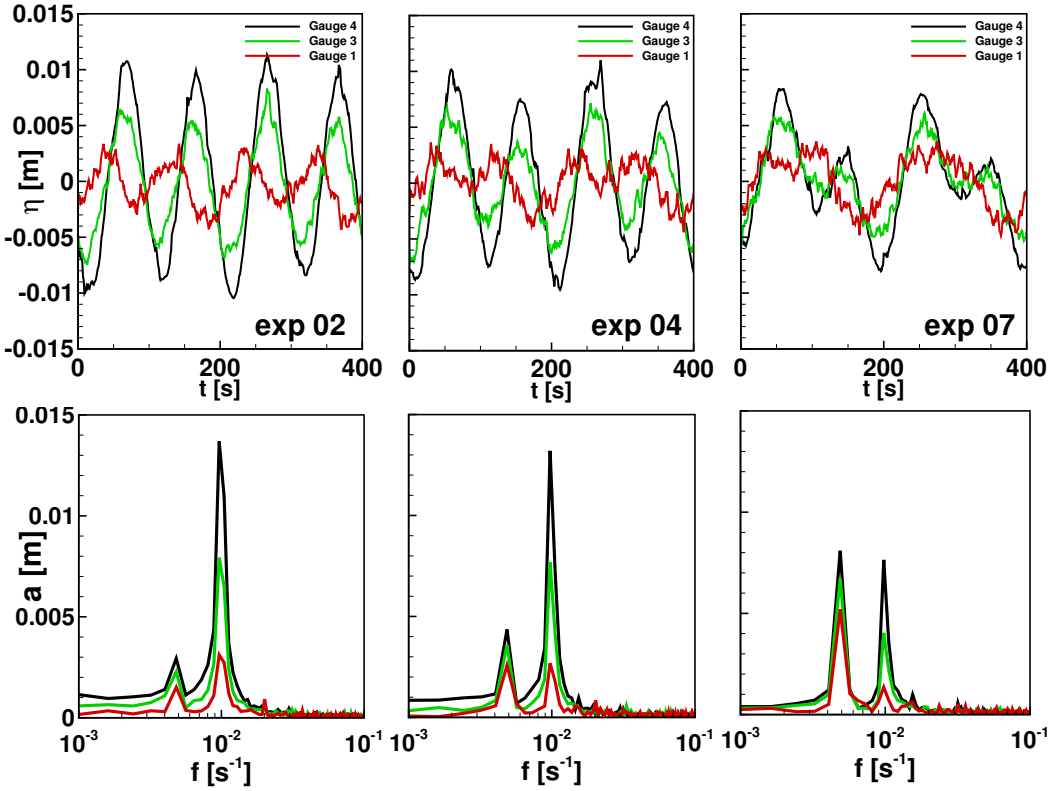

Figure 3. Example of tidal propagation from the flume basin (gauge 1, open sea condition) along the tidal channel (gauge 3 and 4 placed at 14.5 m and 25 m, respectively, from gauge 1) for experiment 2 ($F = 0.2$ semi-diurnal tide), experiment 4 ($F = 0.444$, mixed tide mainly semi-diurnal) and experiment 7 ($F = 1.686$, mixed tide mainly diurnal). Bottom panel, corresponding FFT analysis of the water level signals. The same colors are used for the gauge signals and their corresponding FFT.

4 The effect of multiple tidal harmonics on the time dependent flow and the generation of a residual current

In this section, we discuss the role of the tidal wave shape on the time dependent two dimensional velocity fields $\mathbf{u}(\mathbf{x},t) = (u(\mathbf{x},t), v(\mathbf{x},t))$ measured using the PIV technique. Vortical structures have been identified using the Okubo-Weiss parameter λ_0 (Okubo, 1970; Weiss, 1991), defined as $\lambda_0 = 1/4(S^2 - \omega^2)$, where $S^2 = S_n^2 + S_s^2$ is the total square strain, sum of the normal (S_n) and shear (S_s) components, and ω^2 is the square of the vorticity. Positive values of λ_0 indicate flow regions dominated by shear, whereas negative values of λ_0 indicate the presence of vortices. Here, we are mostly interested to understand how the relative importance of the semi-diurnal and diurnal constituents might influence the generation of flood macro-vortices at the tidal inlet. The generation mechanisms of flood vortices have been subject to several studies in the last years (Wells & van Heijst, 2004; Nicolau del Roure et al., 2009; Vouriot et al., 2019). The driving mechanism has been described in terms of vortex shedding at the corners of the tidal inlet. The generation of flood vortices is only slightly influenced by the shape of the inlet itself (Nicolau del Roure et al., 2009). In the present case, the tidal inlet of the laboratory flume can be classified as a *barrier island* as described in Nicolau del Roure et al. (2009), where the inlet is centered with the tidal channel and the lateral obstructions are thin compared to their length. During the flood phase the flow is forced to enter the

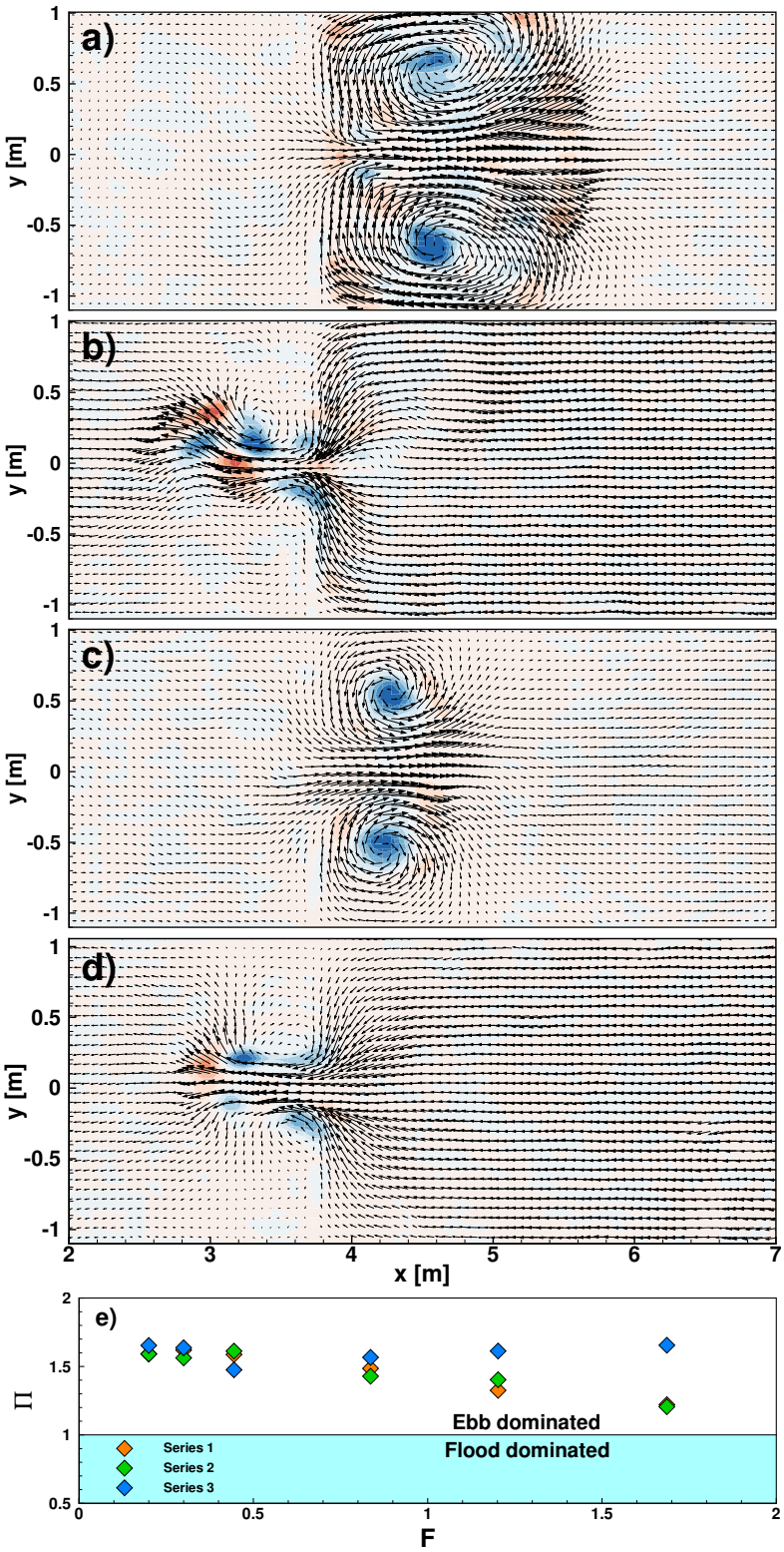

Figure 4. Examples of time dependent two dimensional velocity fields with Okubo-Weiss parameter contours for experiment 5. Panel a) maximum crest flood phase; panel b) and d) flushing ebb phase; panel c) less intense flood. Panel e) Power ratio of ebb and flood powers computed as the time integral of the kinetic energy per unit mass as a function of the form factor F

tidal channel through the inlet and the interaction with the sharp corners generates vorticity that is then stretched and convected towards the channel. The vortex shedding is regulated by the non dimensional frequency described by the Strouhal number $S_t = L/UT$, where L is a typical length scale related to the vortex shedding generation, U is a convective velocity scale and T is the typical tidal period. In this case, the typical tidal period could be considered the period of the dominant tidal constituents and, thus, depends on the form factor F. The flood-macrovortices develop during each cycle and then are found to be flushed out or to remain in the channel depending the values of the Strouhal number (Wells & van Heijst, 2004). A critical Strouhal number has been suggested by Wells and van Heijst (2004) and takes the value of 0.13. For values lower than the critical one, the macro-vortices are expected to be completely flushed out, whereas they do not completely decay and remain confined in the channel close to the inlet for Strouhal greater than 0.13. It is worth noting that the theoretical model of Wells and van Heijst (2004), later confirmed by several Authors (Nicolau del Roure et al., 2009; Vouriot et al., 2019), has been developed for a monochromatic tide in a basin with constant depth. On the contrary, the experimental observations discussed in the companion paper, Part 1, show that the presence of lateral tidal flats are responsible to flush out the flood-vortices regardless the value of the Strouhal number, as reported in other studies with tidal compound channels (Kang & Jun, 2003; Fortunato & Oliveira, 2005). Tidal flats typically induce ebb dominance and this is the main reason for the apparent discrepancy with the cited theoretical and laboratory studies. In the present case, the generation and evolution of the flood-macrovortices is further complicated by a multiple-constituents forcing with different shapes and phase lags of the two harmonics. For very low and high values of the form parameter F, the tides are mainly semi-diurnal and diurnal, i.e. dominated by a single harmonic. In these cases the flood-macrovortices behave in the same way as described in Part 1. More interestingly, in the cases of mixed tides, i.e. for $0.25 < F < 3$, the tidal waves show intermediate crests and troughs. Typical examples of time dependent two dimensional velocity fields with superimposed contours of the Okubo-Weiss parameter λ_0 are shown in Figure 4 panel a) - d), for experiment 5 with $F = 0.836$ and $\phi = 0$. In particular, two different classes of flood-macrovortices are generated depending on the tidal wave crests. In fact, a larger size macrovortices is formed in the flood phase corresponding to the maximum crest, see panel a). The size of the latter structure is comparable to the macrovortices generated in the case of the single harmonic forcing with the same period and relative amplitude. The flood-macrovortices are then flushed away during the ebb phase, see panel b). Secondary macrovortices, the size of which is significantly smaller, typically around half of the primary macrovortices (see panel c)), are generated in correspondence of the second, less intense, tidal crest. Also these second macrovortices are flushed away during the ebb phase. The generation of both primary and secondary vortices is associated to a mechanism of vortex shedding and vortex merging, as already discussed in Part 1. In the supplementary material we provide a movie showing the vortex merging mechanism for the cases of mixed tides, experiment 5. Finite size vortices emitted by the corners of the barrier island are convected by the main flow and embedded in the main macro-structure, increasing its size. A deeper analysis on the Strouhal numbers shows that for values of F lower than 0.6, the Strouhal is higher than the Wells and van Heijst (2004)'s critical value, whereas, for $F > 0.6$, it is lower than 0.13, but also in this case as for the experiments discussed in Part 1, the primary and secondary flood-macrovortices are found to be flushed out towards the basin (open sea). This can be associated to the ebb dominant character of the flow field. Indeed, also for the present experiments, the power ratio $\Pi = P_{ebb}/P_{flood}$, where $P_{ebb}(P_{flood})$ represent the power computed as the time integral of the kinetic energy per unit mass during the ebb (flood) phase, is found to be always greater than 1, see Figure 4 panel e). Interestingly, the power ratio tends to slightly decrease with the form factor F, except for the series 3 ($\phi = \pi/4$). The differences observed among the different series could be explained considering the tidal signals imposed in the three cases. For series 1 and 2 the tidal prism, defined as the amount of water that enters and exits the channel in

a tidal cycle (Fagherazzi et al., 2013), calculated using the imposed water level η would suggest a tendency to have an almost vanishing tidal prism (series 1) and a flood dominated character (series 2). However, the presence of the tidal flats yields to a clear ebb dominance. In the case of series 3, the phase lag $\phi = \pi/4$ generates a stronger asymmetry between the ebb and flood phase, producing an increased ebb dominance of the flow.

A last comment concerns the effect of multiple-constituents on the residual currents generated by the periodic forcing. The importance of the residual currents on the net mass transport has been widely recognized, especially when considering the mixing processes associated to long time transport, i.e. over a time scale of numerous tidal cycles (Valle-Levinson, 2010). As in the companion paper, we have evaluated the steady velocity fields $\mathbf{U}(\mathbf{x}, t)$ by averaging over the total number of tidal cycles recorded during a single experiment. In the present case, however, the tidal wave assumes different shapes depending on the form factor and the possible phase lags. As discussed above, mixed tides generate primary and secondary flood-macrovortices, the latter showing a much smaller typical size. The residual currents, generated by multiple tidal cycles, appear to be quite similar to the ones obtained in the case of monochromatic tides. Examples of residual velocity fields are shown in Figure 5 from panel a) to panel f) for all experiments of series 1. The six shown experiments span the studied range of the form factor F. By inspecting Figure 5, it clearly appears that the shape of the residual currents does not substantially change with F. Averaging over several cycles seems to filter out the secondary flood-macrovortices leaving only the trace of the largest flood-macrovortices. On the contrary, as shown in panel g) of Figure 5, the intensity of the residual current relative to the tidal peak velocity ($|u_p|$) seems to decrease for increasing F both in terms of mean intensity (square symbols) and maximum residual velocities (diamonds symbols). This is in agreement with what observed in the case of monochromatic tides for increasing period and constant relative tidal amplitude. In fact, the diurnal component tends to dominate for increasing form factor and, for constant ϵ, this leads to weaker residual currents. We also observe also that, in the present experiments, the residual currents could reach intensities up to 50% of the peak tidal velocities. The fact that the time dependent velocity fields and the steady components (residuals) assume quite a different behavior could influence the mixing processes. In fact, we expect that the presence of secondary flood-macrovortices in the case of strongly mixed tides could modify the Lagrangian properties of the transport processes.

5 Lagrangian analysis and dispersion regimes

5.1 The influence of the initial conditions on the Lagrangian scale

Following the same approach of the analysis performed in Part 1 for the monochromatic tidal wave, we base the evaluation of the main Lagrangian quantities on the computation of numerical trajectories starting from the two dimensional Eulerian velocity fields. In this section, we will discuss the normalized velocity autocorrelation functions $\mathscr{R}_{uu}$ and $\mathscr{R}_{vv}$, defined as $\mathscr{R}_{uu}(\tau) = (\langle u(t)u(t+\tau)\rangle)/\mathscr{R}_{uu}(0)$ and $\mathscr{R}_{vv}(\tau) = (\langle v(t)v(t+\tau)\rangle)/\mathscr{R}_{vv}(0)$, where the brackets indicate an average over all particle trajectories and τ the time lag. The autocorrelations are then used to evaluate the Lagrangian integral scales T_u and T_v as $T_u = \int_0^{+\infty} \mathscr{R}_{uu} d\tau$ and $T_v = \int_0^{+\infty} \mathscr{R}_{vv} d\tau$ (Taylor, 1921). The Lagrangian integral scale of the process is finally computed as $T_L = 1/2(T_u + T_v)$ that represents the decorrelation time of the dispersion process, i.e. the time required to a tracer particle to loose memory of its initial conditions (position and velocity) (Taylor, 1921; LaCasce, 2008). Differently from Part 1, tidal waves are more complex and their shapes have been varied in the three series of experiments. From an Eulerian point view, the more complex tidal forcing has proven to generate flow structures at different length scales that are periodically generated and destroyed, especially in the mixed tide cases. Since the dynamical processes appeared to be more complicate than in the monochromatic case,

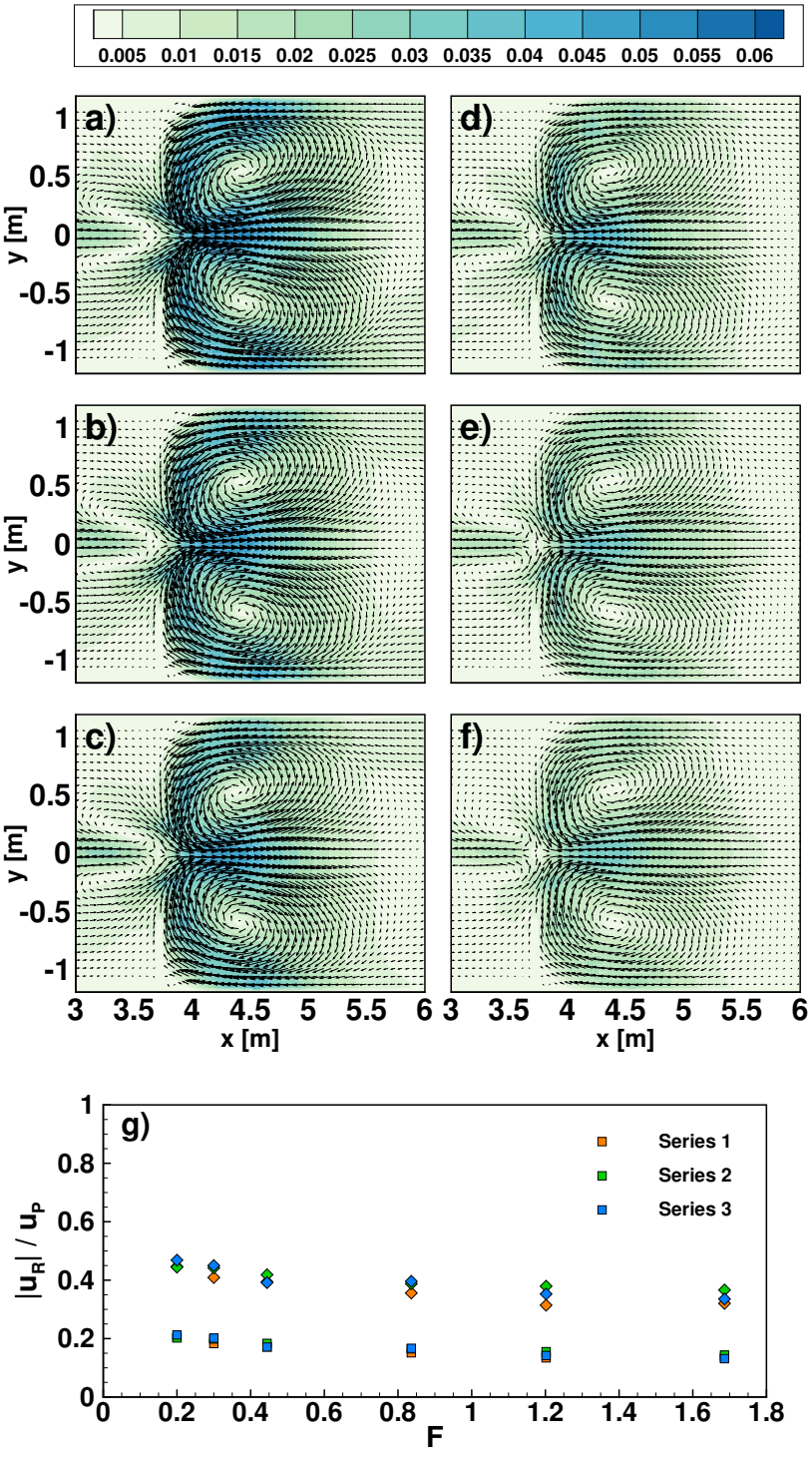

Figure 5. Panel a) to f): examples of residual currents fields for experiments of series 1. g): average residual velocity (squares) and maximum residual velocity (diamonds) divided by the tidal velocity peak at the inlet ($|u_p|$) as function of the form factor F.

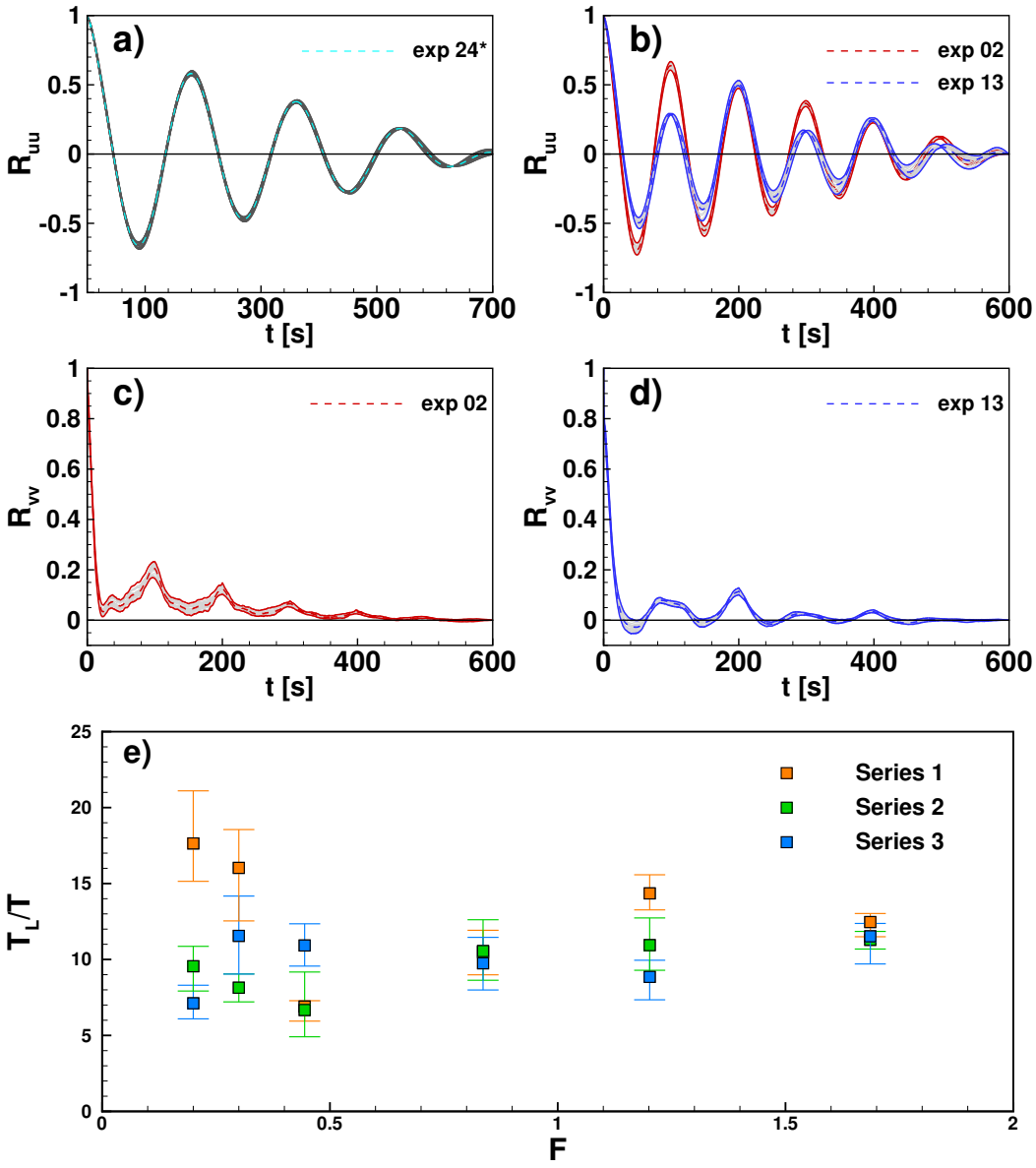

Figure 6. Autocorrelation functions. Panel a) R_{uu} experiment 24 of De Leo et al. Panel b) R_{uu} experiments 2 and 13. Panel c) R_{vv} experiment 2. Panel d) R_{vv} experiment 13. Panel e) non dimensional Lagrangian integral scales as a function of the form factor F. Squared symbols stand for averaged values whereas bars for their spreads.

we have performed a different Lagrangian analysis. In particular, we are interested to understand whether there is an influence of the initial conditions associated to particle release. A similar analysis has been discussed in Enrile et al. (2019), where single and multiple particle statistics have been computed starting from HF-radar total velocity fields of the Gulf of Trieste (Italy), a semi-enclosed coastal basin strongly dominated by tides. When Lagrangian analysis of the kind presented here are performed, the definition of the initial time for particle release is set to coincide with the starting time of the available Eulerian field, which is formally correct when a statistically steady forcing generates the Eulerian flow. We assumed that also for simple monochromatic forcing, exper-

iments of Part 1, the evaluation of the velocity autocorrelations and the integral scales were independent on the initial time of release. On the contrary, for the present experiments we have performed a sequence of Lagrangian computations, releasing the numerical particles at different times during a single wave period (semi-diurnal plus diurnal tidal signals) and, then, we have computed our target functions ($\mathscr{R}_{uu}$, $\mathscr{R}_{vv}$ and the corresponding integral scales) averaging them. In particular, we repeated the computation using 20 initial times, each one separated by a lag equal to $T_d/20$, being T_d the period of the diurnal constituent, which is the period of the wave packet. The results of this procedure are shown in Figures 6a) - d). Grey lines indicate the output of the single run, whereas thick solid lines the lower and higher envelope and the thick dashed line the average functions. Panel a) shows the longitudinal velocity autocorrelation function $\mathscr{R}_{uu}$ for the case of experiment 24, monochromatic tidal case of Part 1, for comparison. As expected there is no influence of the initial conditions of the particle release, all functions are substantially coincident. Panels b), c) and d) show the autocorrelation functions for two experiments, namely experiment 2 (red lines) and 13 (blue lines). The longitudinal velocity autocorrelations (see Figure 6b) show a dependence on the initial conditions only for the values of $\mathscr{R}_{uu}$, without visible modifications of the periodicity of the oscillations. As in the case of the monochromatic tidal waves, the longitudinal autocorrelations have intense negative lobes, which influence the dispersion regimes for time of same order of the Lagrangian time scale. The behavior of the spanwise autocorrelation function $\mathscr{R}_{vv}$, panel c) and d) is more interesting. The subsequent releases produce a wider spread of the autocorrelations values and, more importantly, the negative lobes are likely to appear for particular initial times. It is not simple to relate the different autocorrelation function shapes with the initial times and not particularly relevant: the main point is that particles tend to decorrelate themselves from their initial conditions differently if released at different instants during a multiple constituents tidal period. Moreover, the presence of negative lobes will impact on the computation of the Lagrangian time scales, being the latter the integral of the autocorrelation functions. The resulting Lagrangian integral scales are shown in Figure 6e). The symbols represent the average values of T_L, whereas the bars indicate the spread of the computed values that reach also a considerable percentage of the mean decorrelation time. The Lagrangian scales computed for all the different releases oscillate around a mean value with a periodicity similar to the semi-diurnal period (data not shown), with a behavior similar to the one described in Enrile et al. (2019). As in the case of monochromatic tides, T_L remains always much shorter than the tidal period.

5.2 Absolute dispersion regimes and its dependence on the tidal shape

In the previous section, we have shown how the complex forcing requires a particular attention in the analysis of the decorrelation time scales and how the initial time of the particle release ultimately leads to different autocorrelation functions. We are now interested to analyze the effect on the average dispersion processes in terms of single particle statistics. In fact, starting from the numerical trajectories of particle tracers released uniformly on the domain, we computed the diagonal components of the absolute dispersion tensor as

$$A_{ii}^2\left(t,t_0\right)=\left\langle \left|x_i(t)-x_i\left(t_0\right)\right|^2\right\rangle=\frac{1}{N}\sum_{i=1}^{N}\left|x_i(t)-x_i\left(t_0\right)\right|^2, \tag{4}$$

where the brackets indicate average over the particle ensemble, $x_i(t)$ is the position of the i-th particle at time t that started in position $x_i\left(t_0\right)$ at t_0 , and N is the total number of particles in the ensemble. We then define the total absolute dispersion $a^2(t)$ as the trace of the absolute defined by equation (4) (Elhmaïdi et al., 1993; Provenzale, 1999). The time derivative of $a^2(t)$ is related to the total dispersion coefficient K. It is well known that depending on the time behavior of the total absolute dispersion, $a^2 \propto t^\alpha$, different dispersion regimes can be distinguished. A *diffusive* (or *Brownian*) regime

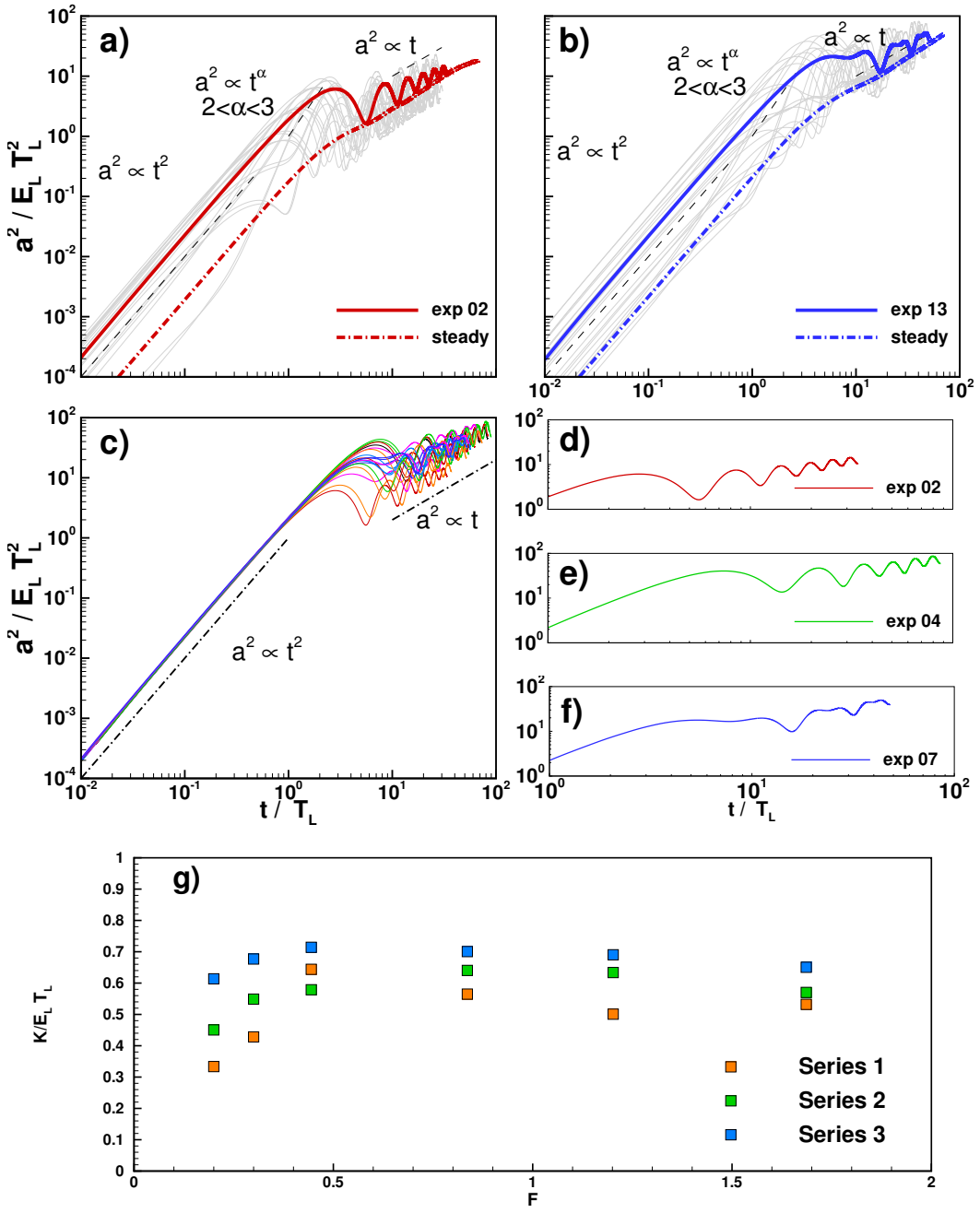

Figure 7. Example of the results obtained from single particle statistics analysis. a) Non dimensional total absolute dispersion as a function of the non dimensional time for experiment 2, b) and experiment 13: grey lines refer to different initial particles releasing, red solid lines to their averaged, red dash-dotted lines indicate the total absolute dispersion inferred from the residual current flow. Regimes are plotted in black dashed lines. c) Averaged total absolute dispersion for all experiments. Focus on linear regimes: d) experiment 2, e) experiment 4 and f) experiment 7. g) Estimated values of the dimensionless diffusion coefficient $K/(E_L T_L)$ as a function of the form factor F.

is found for $\alpha = 1$ and it is associated to a constant diffusion coefficient K (Taylor, 1921). Super (sub)- diffusive regimes are related to exponents greater (smaller) than 1. Sub-diffusive regimes are observed when the velocity autocorrelation functions show a first negative lobe, whose integral is grater than the first positive lobe (Berloff et al., 2002; Veneziani et al., 2004). Looping like correlations are observed in several oceanographic contexts and may be produced by meso-scale vortical structures (Berloff et al., 2002; Veneziani et al., 2004; LaCasce, 2008) or when a periodic forcing as a tide plays an important role (Enrile et al., 2019). Moreover, sub-diffusive regime can be generated by domain characteristics where the flow is generated. In particular, semi-enclosed domain could impose an upper limit for the maximum displacement of the tracer particles respect to their initial position (Artale et al., 1997). On the contrary, a pronounced first positive lobe is usually associated to super-diffusive regime with an exponent α in a range between 2 and 3 (Veneziani et al., 2004), being $\alpha = 2$ the initial ballistic regime for time less than T_L.

A single constituent tidal forcing is able to generate looping like autocorrelation functions and, possibly, leading to super-diffusive regime that appears for time of the order of the Lagrangian integral scales. This regime is a transition between an initial ballistic regime and the asymptotic diffusive regime $a^2 \propto t$, as we have described in the Part 1. In the present case of multiple-constituents, we have performed the calculation of the absolute dispersion using the same strategy as for the autocorrelation functions, i.e. using multiple particle deployment within the longest period (diurnal tide). Typical results of the computation of the total absolute dispersion and the corresponding diffusive coefficients are shown in Figure 7. Note that the total absolute dispersion a^2 and the total diffusive coefficient K have been made dimensionless using the ensemble averaged Lagrangian kinetic energy per unit mass $E_L = 1/2\langle(u_L(\mathbf{x},t)^2 + v_L(\mathbf{x},t)^2)\rangle$ and the Lagrangian integral scale T_L, coherently with the monochromatic experiments. Panels a) and b) show the results of two typical experiments, namely experiment 2 and 13, for the dimensionless $a^2(t)/(E_L T_L^2)$ as a function of the dimensionless time t/T_L. Grey lines represent the output of the single deployment, whereas the solid red line the average over the different releases of the total absolute dispersion. The effects of the initial conditions are clearly visible and produce a bundle of curves that, however, tend to similar regimes for long times. This has been also observed by Enrile et al. (2019) where the spread of the different curves was calculated and a decrease in time was observed. Physically, this suggests that after several tidal cycles the particles are no longer influenced by their initial conditions. However, this further time scale of the process must not be confused with the Lagrangian integral scale T_L that separates the *ballistic* regime from the *Brownian* regime, when the latter exists. Interestingly, all total absolute dispersion curves tend to a diffusive regime for $t/T_L \gtrsim 10$ regardless the initial conditions, which is well described by the averaged $a^2(t)/(E_L T_L^2)$ (red solid line). For $t/T_L \lesssim 1$ a *ballistic* regime is always recovered, whereas super-diffusive regime $a^2(t)/(E_L T_L^2) \propto t^{2\div 3}$ appears only for some particle deployments and this is coherent with the autocorrelation functions that might show intense positive lobes after negative ones, see Figure 6. Moreover, panel a) and b) also report the non dimensional total dispersion evaluated using the residual currents only (dash-dotted lines). As already shown for the single harmonic experiments, the residual currents lead to a time dependence of the total absolute dispersion that substantially filters out the oscillations due to the periodic velocity fields, leaving unaltered the overall slope of the curves. This could demonstrate how the net particle dispersion is produced by the residual currents as claimed in tidal flows (MacCready, 1999; Valle-Levinson, 2010). The total non dimensional averaged dispersion for all experiments are plotted in Figure 7 panel c). Averaging over a great number of initial condition leads to hidden possible super-diffusive regimes and all curves to collapse onto a *ballistic* initial regime. However, we are interested in long time statistics as these describe the typical dispersive regimes that could occur in realistic conditions after many tidal cycles. All experiments shown in panel c) reach an asymptotic diffusive regime with some behaviors related to the shape of the tidal waves. In particular,

the oscillations observed for $t/T_L \gtrsim 10$ depend on the form factor F and show typical periods depending on its values, see Figure 4 panels d)-f) where three experiments are displayed. Experiments 2 and 4 are characterized by tidal waves dominated by the semi-diurnal components, $F = 0.2$ and $F = 0.44$, respectively, whereas experiment 7 corresponds to a mixed tide mainly diurnal ($F = 1.668$). The observed oscillations are coherent with the dominant frequency of the forcing tides.

Finally, we have evaluated the non dimensional total diffusion coefficient $K/(E_L T_L)$ to understand the role of the tidal wave shape. As in the monochromatic case, the greater contribution to $K/(E_L T_L)$ is provided by the longitudinal dispersion, which accounts for more than 95% of its value. As noted in the companion paper and following Besio et al. (2012), it is important to understand which mixing processes are described by the calculated coefficients. In the present case, the residual current has been calculated by taking the average over the tidal periods of the time dependent Eulerian velocity fields and no other decomposition have been performed (Valle-Levinson, 2010). This implies that our procedure yields to the estimate of a total diffusive coefficient ($K = K_x + K_y$) as the sum of a longitudinal coefficient (K_x) and a transverse coefficient (K_y). The latter coefficients include also the turbulent diffusion contribution. This is important when a comparison is attempted with other laboratory and/or field measurements (Fischer et al., 1979; Monismith et al., 2002; Lewis & Uncles, 2003; Banas et al., 2004). Figure 4 panel g) shows the estimated values of the dimensionless diffusion coefficient $K/(E_L T_L)$ as a function of the form factor F. The results suggest that mixed tides enhance the overall longitudinal dispersion with respect to monochromatic tides. In fact, the values of the total non dimensional coefficient show a maximum around $F = 0.5$ and then a slow decrease for increasing F. A second interesting observation regards the effect of the phase lag between the tidal constituents. On average, phase lag $\phi = \pi/4$, namely a lag in the diurnal constituent, produces higher diffusion coefficients. The range of values of $K/(E_L T_L)$ is in agreement with the values obtained for the monochromatic case. A direct comparison with field observations specifically performed to understand the role of the tidal wave shape is complicated by the fact that no information on the typical tides are reported in the studies (Monismith et al., 2002; Lewis & Uncles, 2003; Banas et al., 2004). Following the scaling argument discussed in the companion paper, Part 1, we expect that the non dimensional values of the total diffusion coefficient fall in the observed ranges in real estuaries. However, it would be interesting to verify the tendency of a mixed tide to increase the longitudinal dispersion.

5.3 The interplay of flow structures at different scales.

The analysis of the Eulerian time dependent fields discussed in section 4 has shown that even in a relatively simple geometry, as the one used in the present experimental campaign, flow structures at different scales are generated and, more interestingly, they interact during a tidal cycle. The asymptotic dispersion regime has proven to exist as an average process over the entire domain. In this section, we are interested to discuss the interplay among the particle trajectories and the different scales of the flow. To this end we apply tools commonly reported as multiple particle statistics, see LaCasce (2008) for a review and application to geophysical contexts. Differently from the single particle statistics of section 3, here we follow the separation of couple of particles in time, computing the relative dispersion. The relative dispersion matrix $\boldsymbol{R}^2(t)$ is defined as the mean-square distance at time t between a pair of particles that at time t_0 had a distance equal to r_0:

$$R^2_{ij}(t) = \frac{1}{M-1} \sum_{m=1}^{M-1} \left\{ \left[x_i^m(t) - x_i^{m+1}(t) \right] \left[x_j^m(t) - x_j^{m+1}(t) \right] \right\} \tag{5}$$

where $M-1$ is the number of particle pairs. As for the total absolute dispersion a^2, the total relative dispersion $r^2(t)$ is simply the trace of the relative dispersion matrix $\boldsymbol{R}^2(t)$ and the total relative diffusivity $K^{(2)}(t)$ is its time derivative. Together with the rela-

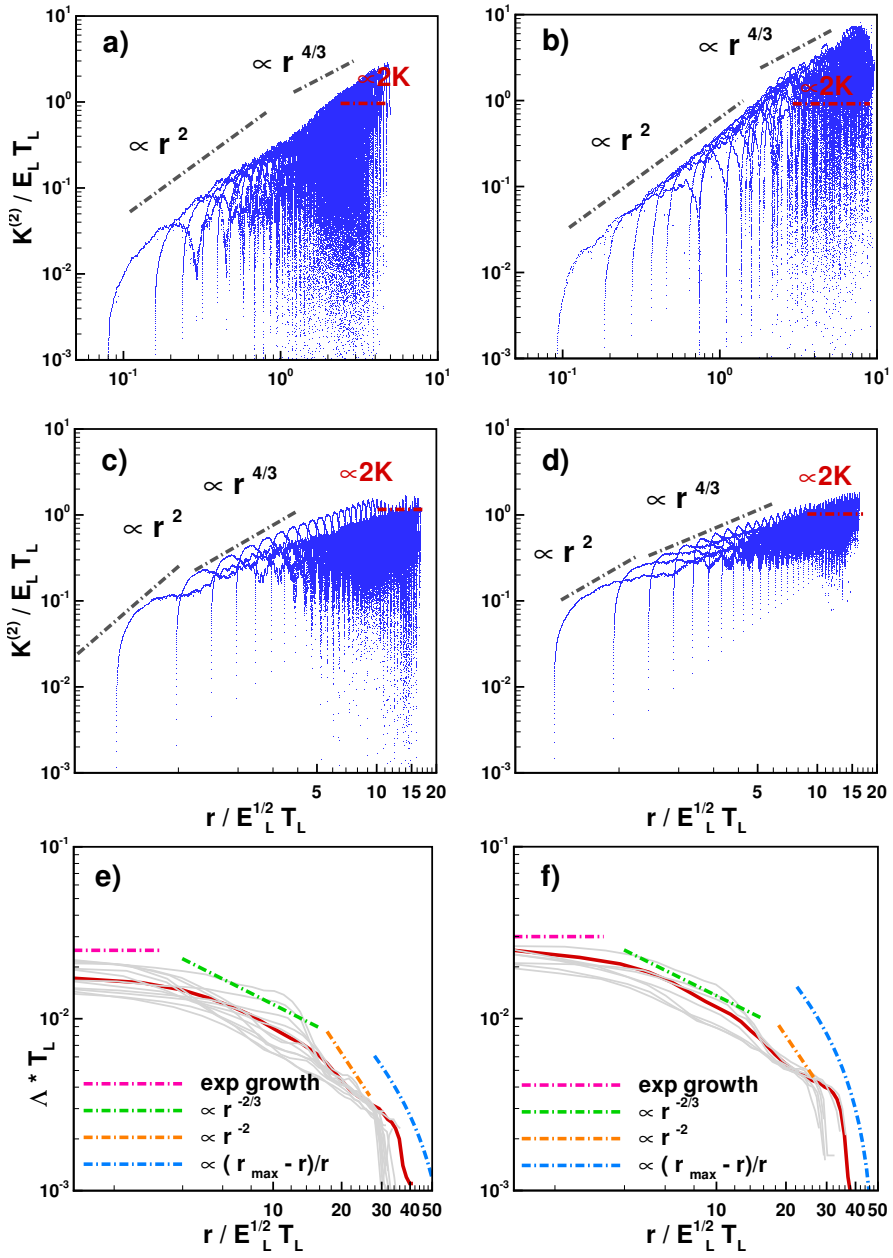

Figure 8. Example of the results obtained from multiple particle statistics analysis. a) dimensionless relative dispersion coefficient as a function of the non dimensional separation of the case of the monochromatic tide experiment number 18. b) same as panel a for the case of the monochromatic tide experiment number 26; c) same as panel a for the experiment 4 of series 1; d) same as panel a for the experiment 13 of series 1; e) non dimensional FSLE as a function of the non dimensional separation for experiment 4 of series 1; f) non dimensional FSLE as a function of the non dimensional separation for experiment 13 of series 1. In each panel the expected theoretical laws are also reported.

tive dispersion, we employ another Lagrangian measure commonly used in dispersion studies, namely the Finite Scale Lyapunov Exponents Λ (FSLE). FSLE consists in average

the times required to a pair to separate from an initial distance to a final one (i.e. Artale et al., 1997; LaCasce, 2008; Cencini & Vulpiani, 2013). Thus, in order to calculate the FSLE it is necessary to first choose a set of distances that are recursively increased as:

$$r_n = \beta r_{n-1} = \delta^n r_0, \tag{6}$$

where n is the chosen number of separation and β is an arbitrary constant larger than unity, and then to calculate the times required (known as "exit time" T_n) for each pair displacement to grow to the successive r_n. At each distance the maximum FSLE is computed as:

$$\Lambda(r) = \frac{1}{\log(\beta)} \left\langle \frac{1}{T_n} \right\rangle, \tag{7}$$

where the brackets indicate an ensemble average over the particle pairs that effectively reach the r_n distance. Care must be taken in the choice of the multiplier δ in order to correctly capture the regimes of the flow at hand (Haza et al., 2008). In our experiments, we set $\delta = 1.2$ as seen in Enrile et al. (2019). Both relative dispersion and FSLE have been extensively used in oceanographic and costal studies leading to a better comprehension of the physical processes at the different separation scales (Artale et al., 1997; Orre et al., 2006; LaCasce, 2008; Haza et al., 2008; Enrile et al., 2018, 2019) . The success of the use of the two measures in geophysical applications relies on classical studies on 2D and atmospheric turbulence (Kraichnan, 1966; Lin, 1972; Er-El & Peskin, 1981; Bennett, 1984; Babiano et al., 1990). The main results were the existence of two distinct dynamical mechanisms leading to two dispersion regimes, namely *local dispersion* and *non-local dispersion* and the link between the scaling law of these regimes with the energy cascade (inverse energy cascade and direct enstrophy cascade). Scaling arguments to describe the different dispersion and energy regimes can be summarized searching for laws of the kind: $K^{(2)} \propto r^{(\alpha+1)/2}$. The link with the energy cascades is the value of the exponent α, having assumed the turbulent energy spectrum as a function of the wave numbers in the form of $E(k) \propto k^{-\alpha}$. Relative dispersion in *local dynamics* is characterized by the effect of local straining, which is not efficient in producing large separation, and the dispersion of pairs is dominated by eddies of the same scale of their separation. This regime is described by values $1 < \alpha < 3$ and, in particular, for $\alpha = 5/3$ the famous Richardson-Obukhov law is recovered with $K^{(2)} \propto r^{4/3}$, that corresponds to the energy cascade $E(k) \propto k^{-5/3}$. On the contrary, *non-local dynamics* is characterized by the effect of vortices with typical scale much larger than the separation. This regime is described by the Kraichnan-Lin law $K^{(2)} \propto r^2$, or more generally for $\alpha > 3$. In this case, the expected energy spectrum corresponds to an enstrophy cascade $E(k) \propto k^{-3}$. Note that where the relative dispersion shows a power law dependence, the FSLEs exhibit a power law dependence on the separation as $\Lambda \propto r^{-2/\gamma}$. The exponent γ is linked to the time growth of r^2 with time (LaCasce, 2008).

The computation of $r^2(t)$, $K^{(2)}$ and $\Lambda(r)$ has been performed on both data sets, single and multiple constituents tides, with the aim to understand which are the typical regimes and if different regimes are triggered by more complex forcing. In the case of multiple constituents we again performed a series of simulations varying the initial time of deployment. Figure 8 shows the typical results for the relative dispersion, the dimensionless relative diffusivity coefficient $K^{(2)}/(E_L T_L)$ as a function of the dimensionless separations $r/(E_L^{1/2} T_L)$, for experiments forced by a single harmonic tide, panel a) and b) (experiment 18 and experiment 26) and for experiments 4 and 13 of the present laboratory campaign, panel c) and d). In the same plots the theoretical laws, namely the Richardson-Obukhov law and the Kraichnan-Lin law, are shown to help the identification of the regimes. It is interesting to note that in all cases, regardless the characteristics of the tidal wave, two distinct regimes can be observed. For separation smaller than a typical injection scale $r_i/(E_L^{1/2} T_L)$, the diffusivity coefficient grows as $K^{(2)}/(E_L T_L) \propto (r/(E_L^{1/2} T_L))^2$, whereas for separation larger than the injection scale the regime follows closely the Richardson-Obukhov law. Correctly for very large separation the growth of the relative diffusivity

coefficient attains a constant value $K^{(2)}/(E_L T_L) \approx 2K/(E_L T_L)$, where $K/(E_L T_L)$ is the total absolute diffusivity coefficient discussed in the previous section. The injection scale $r_i/(E_L^{1/2} T_L)$ is very close to the Lagrangian integral spatial scale. In fact, the change in the relative dispersion regime is close to $r/(E_L^{1/2} T_L) \approx 1$. The two-regime scenario is also confirmed by the trends of the dimensionless FSLE ΛT_L as a function of the dimensionless separation $(r/(E_L^{1/2} T_L))$, see panel e) and f). As for the autocorrelation functions, grey lines indicate the output for the different deployments, whereas the solid lines represent the averaged value. Also in this case we have reported the expected theoretical laws (Artale et al., 1997). The Kraichnan-Lin law previously described is found for $r/(E_L^{1/2} T_L) < r_i/(E_L^{1/2} T_L)$ and implies an exponential growth of the FSLEs. As the separation r increases, the FSLE slope suggests the presence of both the Richardson-Obukhov regime $\Lambda T_L \propto (r/(E_L^{1/2} T_L))^{-2/3}$ and the linear regime $\Lambda T_L \propto (r/(E_L^{1/2} T_L))^{-2}$. Moreover, the FSLE for very large separation exhibits the limiting regime expected for separation close to the saturation length r_{max}, i.e. the maximum separation imposed by the domain. This is typical for semi-enclosed basins as observed in similar geometrical contexts (Artale et al., 1997; Cencini & Vulpiani, 2013; Enrile et al., 2019).

Therefore, the results suggest that *local dispersion* is the dominant process for most of the separation range and, from a physical standpoint, this could be explained by the presence of large scale macro-vortices as the dominant features in all tidal cases so that separations are influenced by local straining produced by the mentioned macrovortices. Moreover, the overall picture seems not to be influenced by tidal wave shape and phase lag between the constituents and this could be explained observing that all the cases are able to trigger similar macro-vortices. Note that the computation of the multiple particle statistics, similarly to the single particle statistics, is averaged over the ensemble of particles deployed uniformly over the domain. This standard procedure relies on the assumption of homogeneity of the flow under investigation (Berloff et al., 2002). Thus, the observed regimes must be considered as the average behavior of the Lagrangian dispersion.

Finally, it is worth noting that the injection separation r_i has been described as of the same order of magnitude of the Lagrangian integral length scale. However, another length scale could play a role in the present experiments, namely the length of the side wall of the tidal inlet l_i. As previously noted, the generation of the flood-macrovortices is controlled by the vortex shedding from the corners of the tidal inlet. This mechanism could be also explained in analogy with the vortex generation downstream a coastal headland, where the extent of the headland is a controlling length scale of the process (Signell & Geyer, 1991; Davies et al., 1995). Two observations might be important for the present case. Firstly, the l_i is very close to the Lagrangian integral spatial scale. Secondly, the flow could be described as a forced turbulence, where the forcing is the presence of the tidal inlet and, thus, l_i could be regarded as the length scale of the injected energy. We clearly observed a vortex merging process that several times is a signature of an inverse energy cascade process. A further piece of information that could confirm this scenario is the presence of two distinct regimes in the relative dispersion and in the FSLE, separated by the injection scale r_i. However, further analyses are required to provide a sound proof of the existence of an inverse energy cascade, which would require the evaluation of the energy spectrum and higher order structure functions (Nikora et al., 2007; Alexakis & Biferale, 2018; Enrile et al., 2020).

6 Conclusions

In the present study, we have reported the main results obtained from an Eulerian and Lagrangian analysis of an extensive laboratory campaign on the dispersion processes generated by tidal waves composed by multiple harmonics. The two dimensional velocity fields measured in a large scale physical model allowed for an analysis of the flow structures generated by complex tidal waves in a geometry that mimics a weakly convergent

and weakly dissipative estuary (Toffolon et al., 2006) open to the sea through a barrier-island type inlet (Nicolau del Roure et al., 2009). It has been observed that the tidal wave shape, represented by the form factor F, and the constituent phase lag strongly influence the generation of the flood-macrovortices in terms of typical length scales. We confirm that the presence of the tidal flats induces the ebb-dominance regardless the typical Strouhal number confirming field observation and in apparent contrast with previous laboratory observation (Wells & van Heijst, 2004; Nicolau del Roure et al., 2009). It is worth noting that a vortex merging mechanism at the tidal inlet has been observed also in the present case as for the single harmonic experiments. Moreover, the residual current seems to be less sensitive to the tidal wave shapes, being very similar to the one generated by a single harmonic tide, as presented in the companion paper. Regarding the Lagrangian properties of the flow, the shape of the tidal waves plays a significant role on the resulting autocorrelation velocity functions as pointed out by the analysis performed varying the initial release time of the particles. On average the total absolute dispersion reached in all cases an asymptotic diffusive regime and the corresponding total diffusivity coefficients K showed a non monotonic trend with the form factor. Mixed tides, mainly semi-diurnal, seem to be more efficient for a longitudinal dispersion. Regrading the multiple particle dispersion processes, both the regimes in the total relative diffusion coefficient and the FSLEs show that the flow is dominated by two regimes for separations lower or greater of a typical injection scale, which seems to be equal to the Lagrangian integral length scale of the lateral extension of the tidal inlet. The Richardson regime of *local dynamics* dominates for a wide range of separation larger than r_i and smaller of a saturation length highlighted in the FSLE trends. Tidal flows are governed by large macro-vortices larger than the mean separation.

The present experiments together with the results discussed in the companion paper, dedicated to the single harmonic tide, have provided a deep understanding of the main dispersion processes occurring in weakly-dissipative estuaries. Two main aspects will require dedicated studies and will be the directions for future insights. Firstly, the role of the flow inhomogeneities that have been hidden so far by the use of Lagrangian statistics based on homogeneous measures (single and multiple particle statistics). Tidal flows have been proved to be able to generate chaotic mixing leading to more complex behaviors (Zimmerman, 1986; Ridderinkhof & Zimmerman, 1992; Orre et al., 2006) that could be interpreted in terms of Lagrangian Coherent Structures (Haller, 2015). Finally, a new dedicated series of experiments, with higher spatial and temporal resolution, will be planned to find an answer to the question whether or not an inverse energy cascade occurs in this class of flows. The possible presence of an inverse energy cascade is quite important also for defining a correct approach in numerical modeling of these important geophysical flows.

Acknowledgments

This research has not been supported by external funding. The Authors declare no conflict of interests. All results are based on large scale PIV measurements, owing to the excessive dimensions of the data set no web repository has been prepared. Data Management Repository available at doi: https://doi.org/10.5281/zenodo.5006407.

References

Alexakis, A., & Biferale, L. (2018). Cascades and transitions in turbulent flows. *Physics Reports*, *767*, 1–101.

Amin, M. (1986). On the conditions for classification of tides. *The International Hydrographic Review*.

Artale, V., Boffetta, G., Celani, A., Cencini, M., & Vulpiani, A. (1997). Dispersion of passive tracers in closed basins: Beyond the diffusion coefficient. *Physics of Fluids*, *9*(11), 3162–3171.

Babiano, A., Basdevant, C., Le Roy, P., & Sadourny, R. (1990). Relative dispersion in two-dimensional turbulence. *J. Fluid Mech.*, *214*, 535-557.

Banas, N., Hickey, B., MacCready, P., & Newton, J. (2004). Dynamics of willapa bay, washington: A highly unsteady, partially mixed estuary. *Journal of Physical Oceanography*, *34*(11), 2413–2427.

Bennett, A. (1984). Relative dispersion: Local and nonlocal dynamics. *J. Atm Sc.*, *41*, 1881-1886.

Berloff, P. S., McWilliams, J. C., & Bracco, A. (2002). Material transport in oceanic gyres. part i: Phenomenology. *Journal of Physical Oceanography*, *32*(3), 764–796.

Besio, G., Stocchino, A., Angiolani, S., & Brocchini, M. (2012). Transversal and longitudinal mixing in compound channels. *Water Resources Research*, *48*(12).

Cai, H., Savenije, H. H., & Toffolon, M. (2012). A new analytical framework for assessing the effect of sea-level rise and dredging on tidal damping in estuaries. *Journal of Geophysical Research: Oceans*, *117*(C9).

Cencini, M., & Vulpiani, A. (2013). Finite size lyapunov exponent: review on applications. *Journal of Physics A: Mathematical and Theoretical*, *46*(25), 254019.

Cucco, A., Umgiesser, G., Ferrarin, C., Perilli, A., Canu, D. M., & Solidoro, C. (2009). Eulerian and lagrangian transport time scales of a tidal active coastal basin. *Ecological Modelling*, *220*(7), 913–922.

Davies, P. A., Dakin, J. M., & Falconer, R. A. (1995). Eddy formation behind a coastal headland. *Journal of Coastal Research*, 154–167.

Elhmaïdi, D., Provenzale, A., & Babiano, A. (1993). Elementary topology of two-dimensional turbulence from a lagrangian viewpoint and single-particle dispersion. *Journal of Fluid Mechanics*, *257*, 533–558.

Enrile, F., Besio, G., & Stocchino, A. (2020). Eulerian spectrum of finite-time lyapunov exponents in compound channels. *Meccanica*, *55*(9), 1821–1828.

Enrile, F., Besio, G., Stocchino, A., Magaldi, M., Mantovani, C., Cosoli, S., ... Poulain, P. (2018). Evaluation of surface lagrangian transport barriers in the gulf of trieste. *Continental Shelf Research*, *167*, 125–138.

Enrile, F., Besio, G., Stocchino, A., & Magaldi, M. G. (2019). Influence of initial conditions on absolute and relative dispersion in semi-enclosed basins. *Plos one*, *14*(7), e0217073.

Er-El, J., & Peskin, R. (1981). Relative diffusion of constant-level balloons in the suthern hemisphere. *J. Atm Sc.*, *38*, 2264-2274.

Fagherazzi, S., Wiberg, P. L., Temmerman, S., Struyf, E., Zhao, Y., & Raymond, P. A. (2013). Fluxes of water, sediments, and biogeochemical compounds in salt marshes. *Ecological Processes*, *2*(1), 1–16.

Fischer, H. B., List, J. E., Koh, C. R., Imberger, J., & Brooks, N. H. (1979). *Mixing in inland and coastal waters*. Academic press.

Fortunato, A. B., & Oliveira, A. (2005). Influence of intertidal flats on tidal asymmetry. *Journal of Coastal Research*, *21*(5 (215)), 1062–1067.

Gisen, J. I. A., & Savenije, H. H. (2015). Estimating bankfull discharge and depth in ungauged estuaries. *Water Resources Research*, *51*(4), 2298–2316.

Haller, G. (2015). Lagrangian coherent structures. *Annual Review of Fluid Mechanics*, *47*, 137–162.

Haza, A. C., Poje, A. C., Özgökmen, T. M., & Martin, P. (2008). Relative dispersion from a high-resolution coastal model of the adriatic sea. *Ocean Modelling*, *22*(1-2), 48–65.

Jay, D. A. (1991). Green's law revisited: Tidal long-wave propagation in channels with strong topography. *Journal of Geophysical Research: Oceans*, *96*(C11), 20585–20598.

Kang, J., & Jun, K. (2003). Flood and ebb dominance in estuaries in korea. *Estuarine, Coastal and Shelf Science*, *56*(1), 187–196.

Kraichnan, H. (1966). Dispersion of particle pairs in homogeneous turbulence. *Phys. Fluids*, *9*, 1937-1943.

LaCasce, J. (2008). Statistics from lagrangian observations. *Progress in Oceanography*, *77*, 1-29.

Lanzoni, S., & Seminara, G. (1998). On tide propagation in convergent estuaries. *Journal of Geophysical Research: Oceans*, *103*(C13), 30793–30812.

Lee, S.-H., & Chang, Y.-S. (2019). Classification of the global tidal types based on auto-correlation analysis. *Ocean Science Journal*, *54*(2), 279–286.

Lewis, R. E., & Uncles, R. J. (2003). Factors affecting longitudinal dispersion in estuaries of different scale. *Ocean Dynamics*, *53*(3), 197–207.

Lin, J. (1972). Relative dispersion in the enstrophy cascading inertial range of homogeneous two dimensional turbulence. *J. Atmos. Sci.*, *29*, 394-396.

MacCready, P. (1999). Estuarine adjustment to changes in river flow and tidal mixing. *Journal of Physical Oceanography*, *29*(4), 708–726.

Monismith, S. G., Kimmerer, W., Burau, J. R., & Stacey, M. T. (2002). Structure and flow-induced variability of the subtidal salinity field in northern san francisco bay. *Journal of physical Oceanography*, *32*(11), 3003–3019.

Nicolau del Roure, F., Socolofsky, S. A., & Chang, K.-A. (2009). Structure and evolution of tidal starting jet vortices at idealized barotropic inlets. *Journal of Geophysical Research: Oceans*, *114*(C5).

Nikora, V., Nokes, R., Veale, W., Davidson, M., & Jirka, G. (2007). Large-scale turbulent structure of uniform shallow free-surface flows. *Environ Fluid Mech.*, *7*, 159–172.

Okubo, A. (1970). Horizontal dispersion of floatable particles in the vicinity of velocity singularities such as convergences. In *Deep sea research and oceanographic abstracts* (Vol. 17, pp. 445–454).

Orre, S., Gjevik, B., & LaCasce, J. H. (2006). Characterizing chaotic dispersion in a coastal tidal model. *Continental Shelf Research*, *26*(12-13), 1360–1374.

Provenzale, A. (1999). Transport by coherent barotropic vortices. *Ann. Rev. Fluid Mech.*, *31*, 55–93.

Ridderinkhof, H., & Zimmerman, J. (1992). Chaotic stirring in a tidal system. *Science*, *258*(5085), 1107–1111.

Seminara, G., Lanzoni, S., Tambroni, N., & Toffolon, M. (2010). How long are tidal channels? *Journal of Fluid Mechanics*, *643*, 479.

Signell, R. P., & Geyer, W. R. (1991). Transient eddy formation around headlands. *Journal of Geophysical Research: Oceans*, *96*(C2), 2561–2575.

Taylor, G. (1921). Diffusion by continuous movement. *Proc. Lond. Math. Soc.*, *20*, 196-212.

Toffolon, M., Vignoli, G., & Tubino, M. (2006). Relevant parameters and finite amplitude effects in estuarine hydrodynamics. *Journal of Geophysical Research: Oceans*, *111*(C10).

Tsimplis, M., Proctor, R., & Flather, R. (1995). A two-dimensional tidal model for the mediterranean sea. *Journal of Geophysical Research: Oceans*, *100*(C8), 16223–16239.

Umgiesser, G., Ferrarin, C., Cucco, A., De Pascalis, F., Bellafiore, D., Ghezzo, M., & Bajo, M. (2014). Comparative hydrodynamics of 10 mediterranean lagoons by means of numerical modeling. *Journal of Geophysical Research: Oceans*, *119*(4), 2212–2226.

Valle-Levinson, A. (2010). *Contemporary issues in estuarine physics.* Cambridge University Press.

Veneziani, M., Griffa, A., Reynolds, A. M., & Mariano, A. J. (2004). Oceanic turbulence and stochastic models from subsurface lagrangian data for the northwest atlantic ocean. *Journal of physical oceanography*, *34*(8), 1884–1906.

Viero, D. P., & Defina, A. (2016). Water age, exposure time, and local flushing time in semi-enclosed, tidal basins with negligible freshwater inflow. *Journal of Ma-*

rine Systems, *156*, 16–29.

Vouriot, C. V., Angeloudis, A., Kramer, S. C., & Piggott, M. D. (2019). Fate of large-scale vortices in idealized tidal lagoons. *Environmental Fluid Mechanics*, *19*(2), 329–348.

Weiss, J. (1991). The dynamics of enstrophy transfer in two-dimensional hydrodynamics. *Physica D*, *48*, 272–294.

Wells, M., & van Heijst, G. (2004). Dipole formation by tidal flow in a channel. In *International symposium on shallow flows. balkema publishers, delft* (pp. 63–70).

Zhang, Z., & Savenije, H. H. (2017). The physics behind van der burgh's empirical equation, providing a new predictive equation for salinity intrusion in estuaries. *Hydrology and Earth System Sciences*, *21*(7), 3287–3305.

Zimmerman, J. (1986). The tidal whirlpool: a review of horizontal dispersion by tidal and residual currents. *Netherlands Journal of Sea Research*, *20*(2-3), 133–154.